

# Upcycling Graphite from Spent Li-Ion Battery with $\text{SiO}_x$ via Mechano-Chemical Process as Next-Generation Anode for Li-Ion Capacitors

Manohar Akshay,<sup>[a]</sup> Mani Ulaganathan,<sup>[b]</sup> Yun-Sung Lee,<sup>\*,[c]</sup> and Vanchiappan Aravindan<sup>\*,[a]</sup>

Hybrid supercapacitors such as Lithium-ion capacitors (LICs) are one of the most modern energy storage devices of great research interest. The hybridization of the battery-type anode with the capacitive-type cathode brings out the synergic effect of enhanced energy density, power capability, long cycle life, and wide operating temperature. Herein, we introduce a simultaneous alloying-intercalation process from the recovered graphite: silicon monoxide (RG:  $\text{SiO}_x$ ) composite as a negative electrode for the LIC applications with the activated carbon (AC) as a counter electrode. The RG from spent lithium-ion batteries is mixed with commercially available  $\text{SiO}_x$  by scalable

mechano-chemical process, *i.e.*, planetary ball-milling, to obtain a high-performance composite with various ratios. The LIC is assembled with an electrochemically prelithiated anode ( $\text{Li}_x\text{Si} + \text{LiC}_6 + \text{Li}_2\text{O}$ ) and paired with AC under balanced mass loading conditions. The LIC delivered a maximum energy density of  $218 \text{ Wh kg}^{-1}$  and power density of  $8.45 \text{ kW kg}^{-1}$  with an ultra-long cycling life of over 20,000 cycles. Remarkably, the energy densities such as 208.7 and  $201.4 \text{ Wh kg}^{-1}$  are observed at various temperature conditions like 10 and  $40^\circ\text{C}$ , respectively, with excellent capacity retention characteristics.

## Introduction

The contemporary world is experiencing an unforeseen change in energy storage and conversion. The non-renewable conventional forms of energy are being replaced with clean and renewable energy sources such as solar, wind, hydrothermal, etc. However, their efficient storage is still in progress and is a topic of discussion. Since 1991, we have had Lithium-ion Batteries (LIBs)<sup>[1–3]</sup> when first introduced by Sony, but they, too, have certain drawbacks. They have been explored and used in several sectors, including electronic devices, transportation, industries, etc. However, these devices still need the required power density for high-end applications. Hence, a futuristic energy storage device that gained momentum recently is lithium-ion capacitors (LICs). These are the next-generation energy storage devices with hybridization of battery-type and capacitor-type electrodes that help to attain high energy and power density in a single device.<sup>[4–7]</sup> Though the studies on

supercapacitors began in the early 1980s, a breakthrough in research started in the early 2000s.

Among the components of the hybrid capacitor, the anode plays a vital role in enhancing electrochemical performance, especially the cycling, charge-discharge rates, energy density, etc. The research on anode started many years back, but the various limitations must be sorted out. Sony used graphite as the anode for LIBs but lacked the specific capacity required for high-end applications. Hence, researchers are interested in developing high-capacity anode material with lower redox potentials ( $< 0.5 \text{ V vs. Li}$ ) and multi-electron reactions by obeying alloying and conversion mechanisms, which is anticipated to perform better than graphite in terms of energy and power capability.<sup>[8–11]</sup> Among the anodes, one of the finest materials is silicon-based derivatives such as silicon metal, silicon monoxide ( $\text{SiO}_x$ ), etc. These materials have a high theoretical capacity (up to  $3578 \text{ mAh g}^{-1}$ ;  $\approx 10\times$  times greater than graphite ( $372 \text{ mAh g}^{-1}$ )), lower redox potential ( $< 0.2 \text{ V vs. Li}$ ), high natural abundance, and extended discharge plateaus.<sup>[12–15]</sup> The significant volume variation ( $> 200\%$ ) during cycling is one of the major issues related to Si-based anodes. These could be overcome using various methods, including making composites with carbonaceous materials, nanostructuring, surface coating, choosing appropriate binders, electrolyte optimization, etc. Silicon-carbon composites can overcome these pulverization issues and improve their electrochemical performance in a better way. That is, the addition of carbonaceous materials can buffer the volume variation of these anodes to a great extent, thereby enhancing the overall electrochemical performance of the LIC.

Among the Si-based derivatives,  $\text{SiO}_x$  is considered a promising electrode for LIC applications owing to the high theoretical capacity of  $2280 \text{ mAh g}^{-1}$  and significantly reduced

[a] Department of Chemistry, Indian Institute of Science Education and Research (IISER), Tirupati, India

[b] Department of Sciences, Amrita School of Physical Sciences, Amrita Vishwa Vidyapeetham, Coimbatore, India

[c] School of Chemical Engineering, Chonnam National University, Gwang-ju, Republic of Korea

**Correspondence:** Dr. Vanchiappan Aravindan, Department of Chemistry, Indian Institute of Science Education and Research (IISER), Tirupati 517619, India.

Email: [aravind\\_van@yahoo.com](mailto:aravind_van@yahoo.com) and [aravind.van@gmail.com](mailto:aravind.van@gmail.com) and [aravindan@iisertirupati.ac.in](mailto:aravindan@iisertirupati.ac.in)

Prof. Yun-Sung Lee, School of Chemical Engineering, Chonnam National University, Gwang-ju 61186, Republic of Korea.

Email: [leeys@chonnam.ac.kr](mailto:leeys@chonnam.ac.kr)

Supporting Information for this article is available on the WWW under <https://doi.org/10.1002/cssc.202400822>

volume variation, compared to the pristine Si, due to the presence of oxygen.<sup>[16]</sup> Despite that, the challenges still need to be addressed are the lower electronic conductivity, capacity fading, and poor solid electrolyte interphase (SEI). In addition, the reaction of  $\text{SiO}_x$  with lithium results in significant lithium loss and lower initial coulombic efficiency due to the formation of inert lithium oxides and silicates ( $\text{Li}_2\text{O}$ ,  $\text{Li}_4\text{SiO}_4$ , etc.). Major issues can be resolved using carbonaceous materials as the composites, as it enhance the electrical conductivity, buffer volume changes, and stabilize the SEI layer. We have prepared the recovered graphite<sup>[17]</sup> (RG, from spent LIBs):  $\text{SiO}_x$  composite as anode for our LIC by simple planetary ball-milling technique. Many previously reported works on using carbonaceous materials, such as  $\text{SiO}_x$  composite, as an anode for LIBs exist.<sup>[18–22]</sup>

Recycling and repurposing the spent/dead LIB has gained attention in the very recent past only, in which anodic recovery is least considered when compared to cathodes<sup>[23–25]</sup> as it is not economically viable. However, we believe recovery is very important in the present scenario as the demand for LIBs increases and so as generating wastes. Our work will be a small step towards the waste-to-wealth approach by adopting the direct recycling process. To the best of our knowledge, we are the first ones to report on the formulation of composite, with alloy-type  $\text{SiO}_x$  and the recovered graphite from spent LIBs, as an anode in the pre-lithiated form for LICs with non-Faradaic AC as a counter electrode. The interesting fact about the usage

of the RG is the expanded interlayer spacing, which is beneficial in terms of achieving the high power performance of the systems. Our previous works on the fabrication of the LIC and Na-ion capacitor assemblies convincingly proved the expanded interlayer spacing of the RG.<sup>[26,27]</sup> This work employed the most straightforward method for synthesizing the RG:  $\text{SiO}_x$  composite. Various ratios of two active materials (RG &  $\text{SiO}_x$ ), which undergo the intercalation and alloying reactions with Li, are mixed well with a mechanical planetary ball miller and are directly employed as the anode for LIC with a commercially available AC cathode under the balanced mass loading conditions. The half-cell and full-cell studies exhibited superior cyclic stability, energy & power density and are compatible with different environment conditions, analyzed from temperature studies.

## Results and Discussion

### Material Characterization

All the composites were synthesized using a scalable planetary ball-milling technique. The crystal structure of all the composites was examined using the powder X-ray diffraction (XRD) measurement, and the patterns are given in Figure 1a. The crystalline nature of RG is well depicted in the XRD pattern with sharp identical graphitic peaks at  $26.47^\circ$  corresponding to the

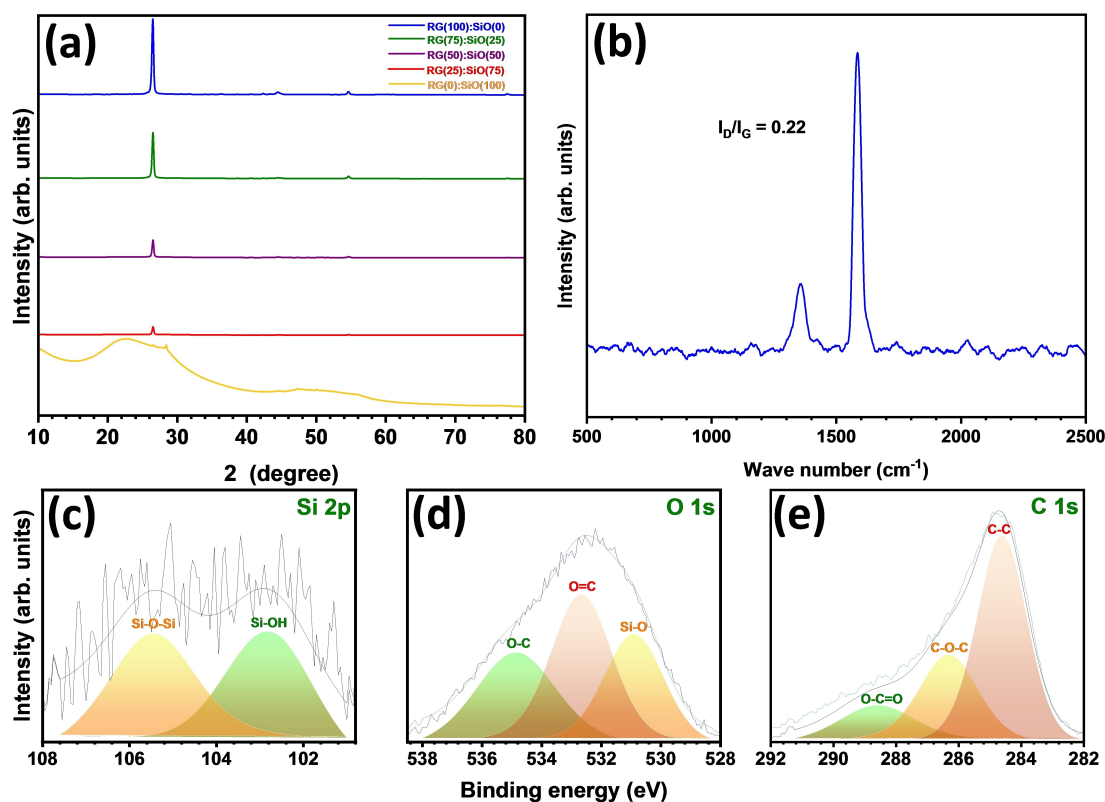


**Figure 1.** Physical characterization of RG(75):SiO(25) composite: (a) XRD patterns, (b) Raman spectrum. Deconvoluted XPS spectra of the composite: (c) Si 2P, (d) O 1s, and (e) C 1s.

(002) plane (Figure S1). The peaks correspond to the hexagonal crystal structure ( $a=b=2.46 \text{ \AA}$ ,  $c=6.74 \text{ \AA}$ ;  $\alpha=\beta=90^\circ$ ,  $\gamma=120^\circ$ ) with 194 : P63/ mmc space group (DB card number: 04-014-0362). The broad peaks of the  $\text{SiO}_x$  at  $22.47^\circ$  and  $50^\circ$  explains its amorphous nature. It is observed that the intensity of the graphitic peak reduces as we shift from the concentration of RG 100% to  $\text{SiO}_x$  100%, which is common. The average crystalline size of the RG(75): $\text{SiO}_x$ (25) composite was calculated from the XRD peaks, and a value of 22 nm was obtained. In addition, for the three composites, except RG 100% and  $\text{SiO}_x$  100%, all the peaks correspond to either RG or  $\text{SiO}_x$ , which confirms the purity of the phase synthesized. Apparently, no oxidation happens during the ball-milling process.

The texture of all the composites was examined from the nitrogen adsorption/desorption studies (Figure S2). Among the composite, the RG 100% exhibited the maximum surface area of  $8.2 \text{ m}^2 \text{ g}^{-1}$ , and a slight depletion in surface area was observed with the increase of  $\text{SiO}_x$  content (Table S1 of the supplementary section). The RG(75): $\text{SiO}_x$ (25) composite has a sufficiently good BET (Brunauer–Emmett–Teller) surface area of  $6.2 \text{ m}^2 \text{ g}^{-1}$  with pore volume and pore radius around  $0.053 \text{ cc g}^{-1}$  and  $16.6 \text{ \AA}$ , respectively, which catalyzes the overall electrochemical performance of the LIC. Figure 1b displays the Raman spectra of the RG(75): $\text{SiO}_x$ (25) composite, showing characteristic peaks at  $\sim 1359$  and  $\sim 1585 \text{ cm}^{-1}$  corresponding to the D and G bands of the RG. The D-band or defect/dispersive band indicates the structural imperfections in graphite lattice either as a result of the long-term cycling of LIB or during the recovery/synthesis process. This peak indicates that the graphite we used for our study is recovered with structural defects to a small extent. In contrast, the G-band (graphite band) is a significant band of graphite that corresponds to the in-plane stretching of  $sp^2$  carbons in its hexagonal lattice. The degree of disorder or graphitization can also be analyzed from the ratio of intensities of the D-band and G-band.  $I_D/I_G$  gives us an idea of how disordered the graphite is. Before ball-milling, the RG

displayed a value of 0.04 and slightly increased to 0.22 after ball-milling, indicating that the ball-milling caused slight disorderliness in the graphitic structure (Figure S3). The surface chemistry analysis of the RG(75): $\text{SiO}_x$ (25) composite was performed carefully using the XPS studies. The elements such as C, O, and Si were detected from the XPS survey, and the corresponding illustration is given in Figure 1(c–e). The Si 2P spectrum is deconvoluted into two peaks at binding energies 102.85 and 105.45 eV, corresponding to Si-OH and Si-O-Si bonding, respectively. Similarly, O 1s is deconvoluted into three peaks at binding energies of 530.9, 532.6, and 534.8 eV, corresponding to the Si-O, O=C, and O-C bonding, respectively. The later two peaks arose due to the graphitic oxidation when exposed to air. The former peak indicates the bonding of O in the  $\text{SiO}_x$ . The C 1s is also deconvoluted into three peaks at binding energies 284.6, 286.3, and 288.6 eV corresponding to the C-C, C-O-C, and O-C=O bonds of C, respectively.

Surface morphological features of the RG(75): $\text{SiO}_x$ (25) composite were examined using field emission-scanning electron microscopy (FE-SEM). The composite mixture of flaky graphite with nanosized particulate  $\text{SiO}_x$  can be observed from the SEM images at different magnifications in Figure 2(a–c). The additional images of the composite in the supplementary section (Figure S4 (a–c)) also show the flakes of graphite arranged in a flower-like morphology. The other composites' morphology was also studied and given in the supplementary section (Figure S5). The RG: $\text{SiO}_x$  composites can be well distinguished from the composition of the flaky and particulates in the SEM images. The increase/decrease in particulate/flaky morphology can be observed as the  $\text{SiO}_x$ /RG percentage increases/decreases. The post-cycling analysis of the abovesaid composite was also performed, showing the morphology change due to the continuous cycling (Figure S6).

Further magnification was performed using the high-resolution transmission electron microscope, where the morphology and internal structure were examined. The lattice

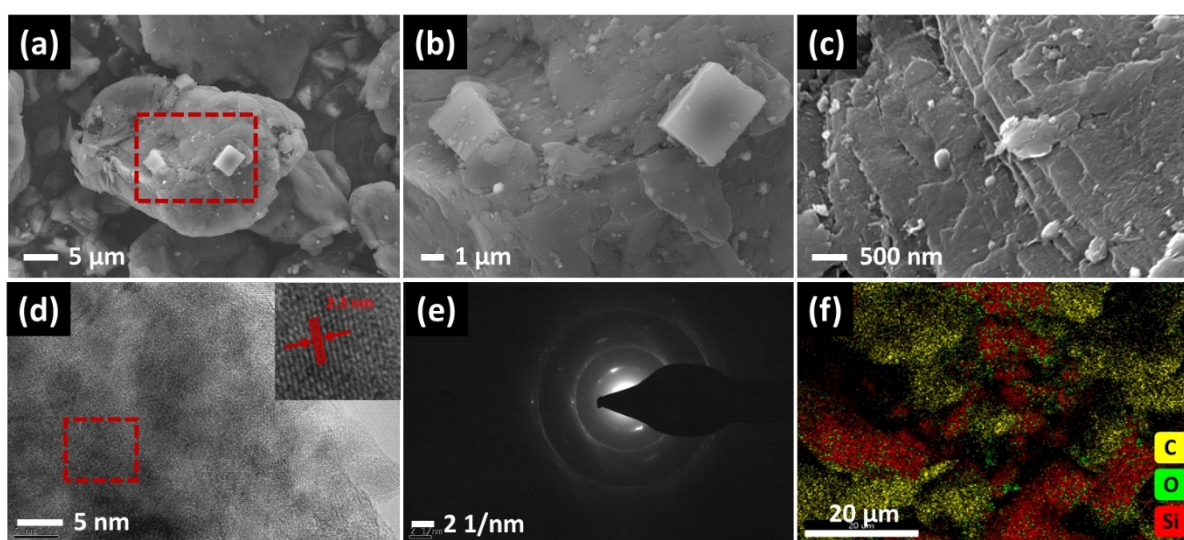


**Figure 2.** (a–c) FE-SEM images of the RG(75): $\text{SiO}_x$ (25) composite at three different magnifications, (d) HR-TEM image, (e) SAED pattern, and (f) EDS elemental mapping of the composite.

fringes can be observed in the Figure 2d, and the  $d$ -spacing is calculated to be 2.3 Å. The crystallinity was further confirmed by the concentric diffraction rings of the SAED pattern in Figure 2e. The energy dispersive X-ray spectroscopy (EDS) elemental mapping confirmed the chemical composition and purity of the composite (Figure 2f). It displays the presence of the C, Si, and O elements with their homogenous distribution. The presence of increased graphitic content (75% of RG) was asserted from the additional EDS mappings given in the supplementary section (Figure S4 (d–f)), which was indicated by the yellow colour. In addition, the EDS analysis was also performed for the composite after cycling, as shown in Figure S6 (d–f).

### Electrochemical Studies

Galvanostatic and potentiostatic methods were employed to study Li-storage properties in RG:SiO<sub>x</sub> composite as an insertion and alloy-type anode. Firstly, the cyclic voltammetry (CV) analysis was carried out for all the composites, and the electrochemical performances were analyzed. All composites were swept between 0.005 and 2.5 V vs. Li at a scan rate of 0.1 mVs<sup>−1</sup> for six cycles (Figure S7), where the second cycle of all the composites was given in Figure 3a. The RG(100): SiO(0) shows prominent cathodic peaks at ~0.17 V, 0.07 & 0.01 V vs. Li, indicating the Li-intercalation to the graphite layers by the

staging process (LiC<sub>12</sub> to LiC<sub>6</sub>)<sup>[28]</sup> and the formation of Li-intercalated complex LiC<sub>6</sub> ( $Li + 6C \rightarrow LiC_6$ ). The anodic peaks at ~0.15, 0.21, & 0.25 V, vs. Li corresponds to the de-intercalation/extraction of Li<sup>+</sup> from the binary graphite intercalation compound, LiC<sub>6</sub> ( $LiC_6 \rightarrow 6C + Li$ ). The CV traces overlap for  $n$  number of cycles, which indicates the structural integrity of the layered structure of the RG. The other four composites (RG(75): SiO(25), RG(50): SiO(50), RG(25): SiO(75)) and RG(0): SiO(100)) have prominent cathodic peaks observed at 0.1, 0.11 and 0.15 V vs. Li, respectively, denote the structural destruction, electrolyte decomposition followed by the formation of the irreversible SEI layer. Also, the alloying of the reaction of Si also takes place ( $SiO_x + Li \rightarrow Li_{3.75}Si + Li_2O$ ) within the potential (<0.3 V vs. Li). The anodic peaks observed ~0.5 V vs. Li are associated with the de-alloying reaction ( $Li_{3.75}Si \rightarrow Si^0 + 3.75Li$ ). The rate capability was also examined by scanning at different scan rates ranging from 0.1 to 1 mV s<sup>−1</sup> and is also given (Figure S8).

All the composites were subjected to galvanostatic charge-discharge in the potential window of 0.005 to 2.5 V vs. Li at a current density of 0.1 Ag<sup>−1</sup> except the RG(100): SiO(0) composite, where the potential window is shrunk to 0.005 to 2 V vs. Li. The plot showing the first cycle of all the composites is given in the supplementary section (Figure S9). The second cycle of the long-term of all the composites given in Figure 3b shows the specific charge/discharge capacities. As expected, the RG(0): SiO(100) shows the highest initial charge/discharge capacity (1143/1350 mAh g<sup>−1</sup>), and RG(100):SiO(0) (308/308 mAh g<sup>−1</sup>) ex-

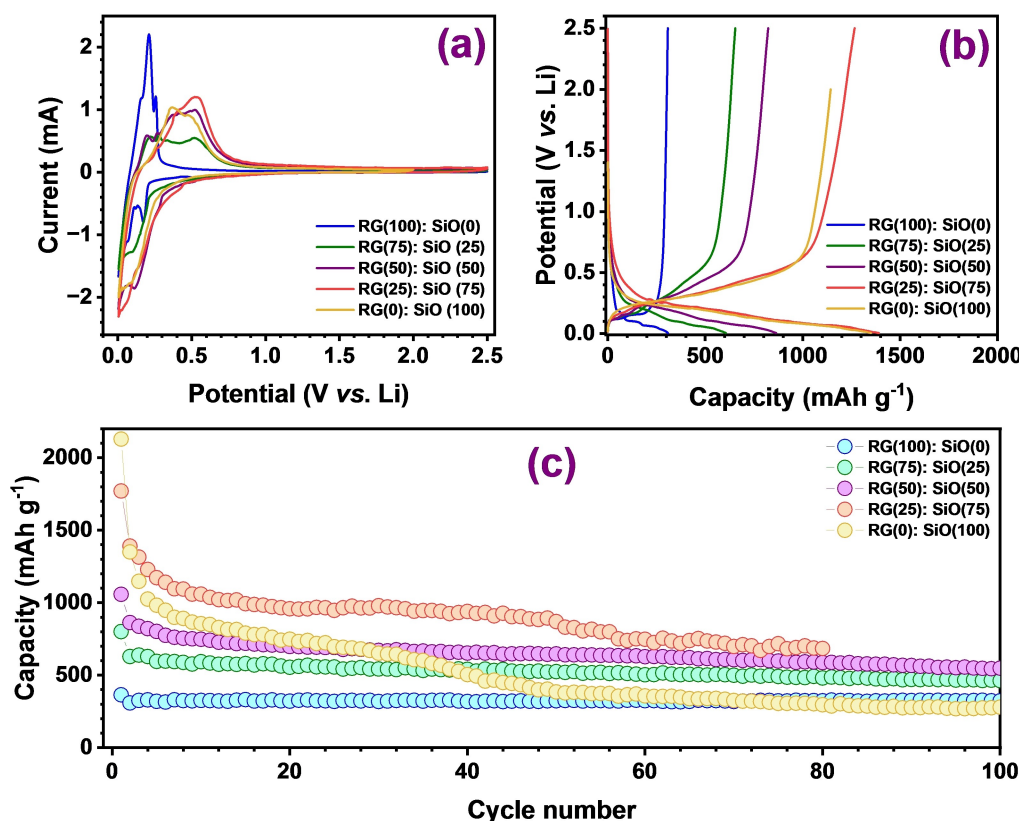


**Figure 3.** (a) Cyclic voltammogram (CV) comparison of all the five composites (second cycle), (b) second cycle charge-discharge profile of the composites, and (c) cycling performance of all the composites.



hibits the lowest. It is worth mentioning that the former undergoes only the alloying/de-alloying reaction, while the latter undergoes the insertion/extraction process only. In the case of the composites, both insertion and alloying mechanisms are simultaneously occurring, and the initial cycle charge/discharge capacity decreases as the RG percentage increases. The specific charge/discharge capacities of RG(75):SiO(25), RG(50):SiO(50) and RG(25):SiO(75) composites are 654/606, 823/863 and 1266/1391 mAh g<sup>-1</sup>, respectively. Nothing out of the box was observed for the composites in the initial cycles, but as the cycle progresses, we could observe that the high percentile SiO<sub>x</sub> composites destabilize faster. All three composites undergo simultaneous insertion/extraction and alloying/de-alloying reactions with respect to the concentration of the RG and SiO<sub>x</sub>. The RG(75):SiO(25) and RG(50):SiO(50) composites exhibit better stability and reversibility during cycling, which

can be clearly observed in Figure 3c. The discharge capacity exhibited by these RG(0):SiO(100), RG(50):SiO(50), RG(75):SiO(25), and RG(100):SiO(0) composites are found to be 279, 548, 462, and 323 mAh g<sup>-1</sup>, respectively with high coulombic efficiencies. The RG(25):SiO(75) composite, similar to RG(0):SiO(100), shows fast degradation as the cycling progresses and exhibits a discharge capacity of 684 mAh g<sup>-1</sup> after 80 cycles. This is mainly because the presence of carbonaceous content in the composite is insufficient to sustain the volume variation observed during the alloying reaction of the SiO<sub>x</sub>. However, better electrochemical profiles are noted for the case of the RG(50):SiO(50), and RG(75):SiO(25) composites.

Figure 4 displays the rate capability study with coulombic efficiency of the five composite anodes from the current density of 0.05 to 1.5 A g<sup>-1</sup>. Generally, as the current rate increases, the specific capacity decreases. The same trend is observed in all

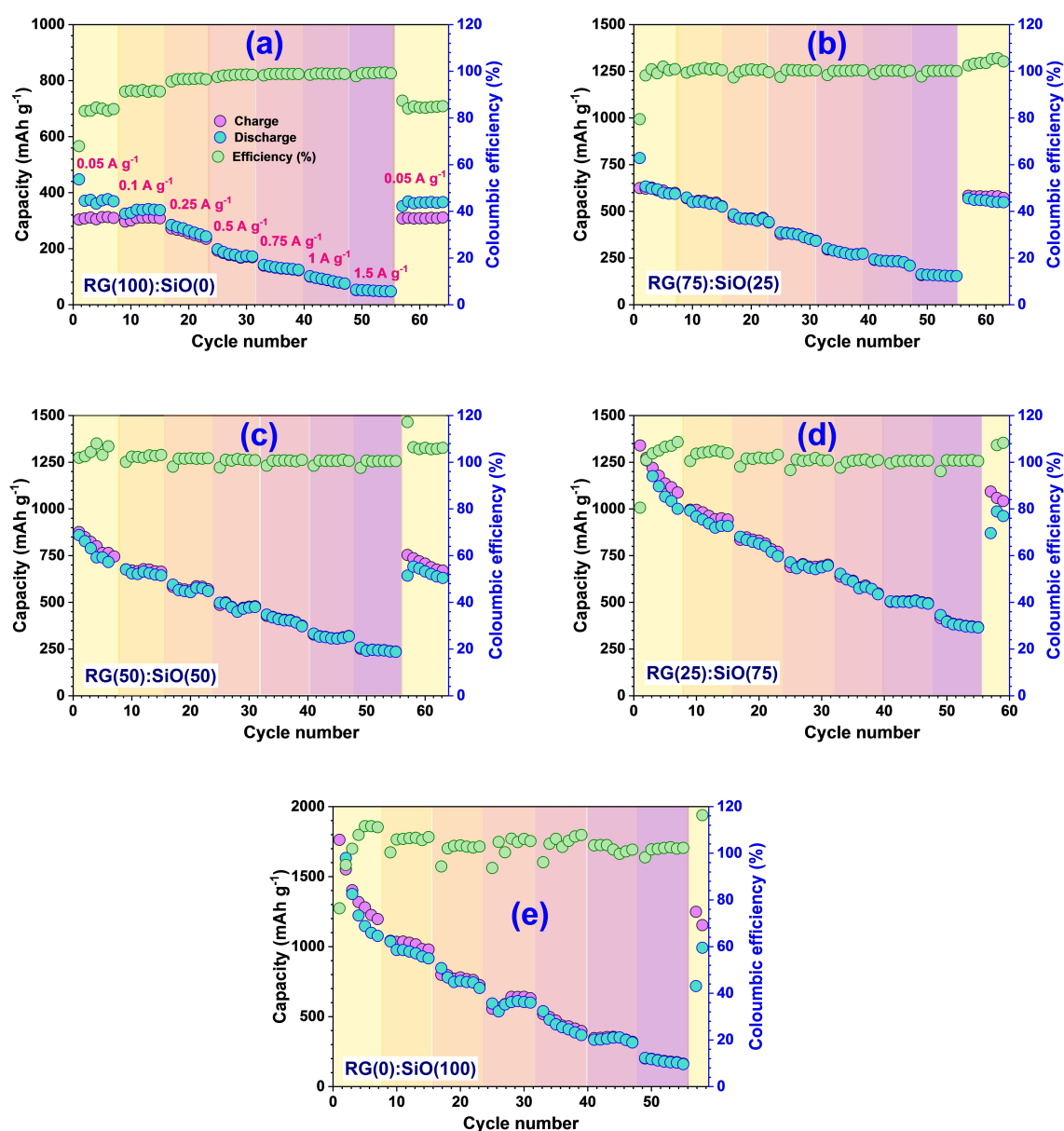


**Figure 4.** Capacity vs. cycle number plots with coulombic efficiency of all the five composites at different current densities (0.05 to 1.5 A g<sup>-1</sup>).

the composites, irrespective of the mechanisms. However, when the current density is again reduced to  $0.05 \text{ Ag}^{-1}$ , an excellent capacity retention behaviour is observed for RG(75):SiO(25) composite compared to the other composites. Moreover, about 91 % of capacity retention was exhibited when the current density was reduced to minimal. The cell displayed a reversible capacity of  $\sim 610 \text{ mAh g}^{-1}$  at  $0.05 \text{ Ag}^{-1}$  and maintained the capacity of  $\sim 156 \text{ mAh g}^{-1}$  even at the current density of  $1.5 \text{ Ag}^{-1}$ . The coulombic efficiency during the cycling was also evaluated and is observed to be above 97 %, which displays the composite's excellent reversibility and electrochemical stability.

A passivation layer formed on the composite anode of the LIC during initial cycling called the SEI layer. This layer plays a vital role in the cyclability, rate performance, initial irreversible capacity fading, and even the LIC's safety. The quality and robustness of the layer were measured using a simple electrochemical *in-situ* impedance spectroscopic study. The impedance for Li/RG(75):SiO(25) cell was measured with an applied ac amplitude of 10 mV at different potential intervals in the working-potential window for 100 cycles (Figure 5 & Figure S10). The prominent semicircle traces were observed for all cycles in the high and mid-frequency region, indicating the interfacial resistance ( $R_{\text{SEI}}$ ) and charge transfer resistance ( $R_{\text{CT}}$ ) between the electrode and electrolyte. The high initial  $R_{\text{CT}}$  value and the large radii semicircle at the lower potential in the first cycle depict the SEI layer formation. However, advancement in cycles decreases the semi-circular area, corresponding to the stabilization of the SEI layer. Specifically, at the 100<sup>th</sup> cycle, different potential semicircles are almost identical, which infers the stability of the formed SEI layer. Hence, this study implies, and we believe, that the enhanced electrochemical performance of our LIC is primarily due to the robust SEI layer.

The composite anodes were packed with the commercial AC cathode to fabricate the hybrid LIC. The Li/AC half-cell was tested between 1.5 to 4.5 V vs. Li at a current density of  $0.1 \text{ Ag}^{-1}$  for more than 400 cycles (Figure S11). The linear behaviour of the charge-discharge profile indicates the non-faradaic nature of the charge storage mechanism. For such a wide testing potential window, Li/AC cells during the charging process will adsorb the  $\text{Li}^+/\text{PF}_6^-$  ions over the anode/cathode, respectively, and during discharge, it will be desorbed. Our LIC comprises two electrodes with different charge storage mechanisms: Faradaic over the anode and non-Faradaic over the cathode. The LIC is fabricated so the anode (Li/RG:SiO<sub>x</sub> composites) is initially pre-lithiated ( $\text{LiC}_6 + \text{Li}_{3.75}\text{Si} + \text{Li}_2\text{O}$ ) by charge-discharge for a few cycles and the cell is terminated at the third discharge. The cell is dismantled in the lithiated state and is paired with the mass-balanced AC cathode loading to get the LIC assembly. Mass-balancing is another critical step in the fabrication of hybrid LIC, as a kinetic imbalance between electrodes exists due to the two different charge storage mechanisms.

The hybrid nature of the LIC was confirmed by the CV comparison studies of anodic half-cell (Li/RG(75):SiO(25)), cathodic half-cell (Li/AC), and full cell (AC/(LiC<sub>6</sub> + Li<sub>x</sub>Si + Li<sub>2</sub>O), LIC), as shown in Figure S12. All the composites in the full-cell

assembly were subjected to galvanostatic charge/discharge at different current densities, given in Figure 6(a–e). Out of all the five composites, undoubtedly superior performance was exhibited by the RG(75):SiO(25), which is evident from the  $E_{\text{cell}}$  vs. time graph (Figure 6b) and Ragone plot (Figure 6f). The AC/RG(75):SiO(25) LIC with anodic and cathodic masses of 1.92 and 11.08 mg delivered a maximum energy density of  $218 \text{ Wh kg}^{-1}$  and power density of  $8.45 \text{ kW kg}^{-1}$ . Compared to LIC with bare RG (Max. energy density =  $163.3 \text{ Wh kg}^{-1}$  & max. power density =  $7.5 \text{ kW kg}^{-1}$ ) and SiO<sub>x</sub> (Max. energy density =  $212.5 \text{ Wh kg}^{-1}$  & max. power density =  $8.3 \text{ kW kg}^{-1}$ ), the performance of RG(75):SiO(25) composite is impressive. We strongly believe that the synergic effect of both intercalation and alloying reactions in RG(75):SiO(25) composite-based LIC brings out the best performance to attain the highest energy and power density out of all the composites at all the current densities. Even at a high current density of  $2.5 \text{ Ag}^{-1}$ , a satisfactory energy density of  $33.5 \text{ Wh kg}^{-1}$  is achieved. These magnificent performances of LIC open the door to the practical application of the composite, as achieving higher energy density at higher current rates is one of the primary prerequisites for the practical application. In addition, the long-term cycling performance of LICs is another prime aspect of commercialization. Our LIC was also subjected to charge-discharge at a high current rate ( $0.75 \text{ Ag}^{-1}$ ) for more than 20,000 cycles. Figure 6g displays the capacity retention vs. cycle number plot, showing the excellent performance of the LIC with a capacity retention of  $\sim 72\%$  after 20,000 cycles, which is very close to the practical application regime. Further enhancement of our LIC's performance is in progress to bring our LIC into the commercial market.

We also explored the possibility of utilising the AC/RG(75):SiO(25)-based LIC assembly at different climatic conditions. The LIC exposed to different temperatures (10, 25, and  $40^\circ\text{C}$ ) exhibited excellent rate performance and cyclic stability (Figure 7). The LIC's energy density and power density values at high and low temperatures are very close to the room temperature value. The power density value of the LIC is found to be maximum at  $40^\circ\text{C}$  because of the increased activity of electrolytes at high temperatures (Figure 7d). From the long-term cyclic study, we could observe decent capacity retention of 72.3 % at  $25^\circ\text{C}$  and 88.4 % at  $40^\circ\text{C}$  after 1000 cycles. However, we could observe the capacity degradation at  $10^\circ\text{C}$ , which could be due to the freezing of the electrolyte at lower temperatures (Figure 7e). Overall, the performance of AC/RG(75):SiO(25) LIC was remarkable at different temperatures and current rates. This displays the compatibility of the LIC with different climatic conditions, which smooths the way for practical applications.

## Conclusions

In summary, we have developed a high-performing LIC with a composite of graphite recovered from spent LIBs and commercial SiO<sub>x</sub> as an anode and commercially available activated carbon cathode. The RG:SiO<sub>x</sub> composites were made by mechanical milling and directly used as the anode for the LIC.

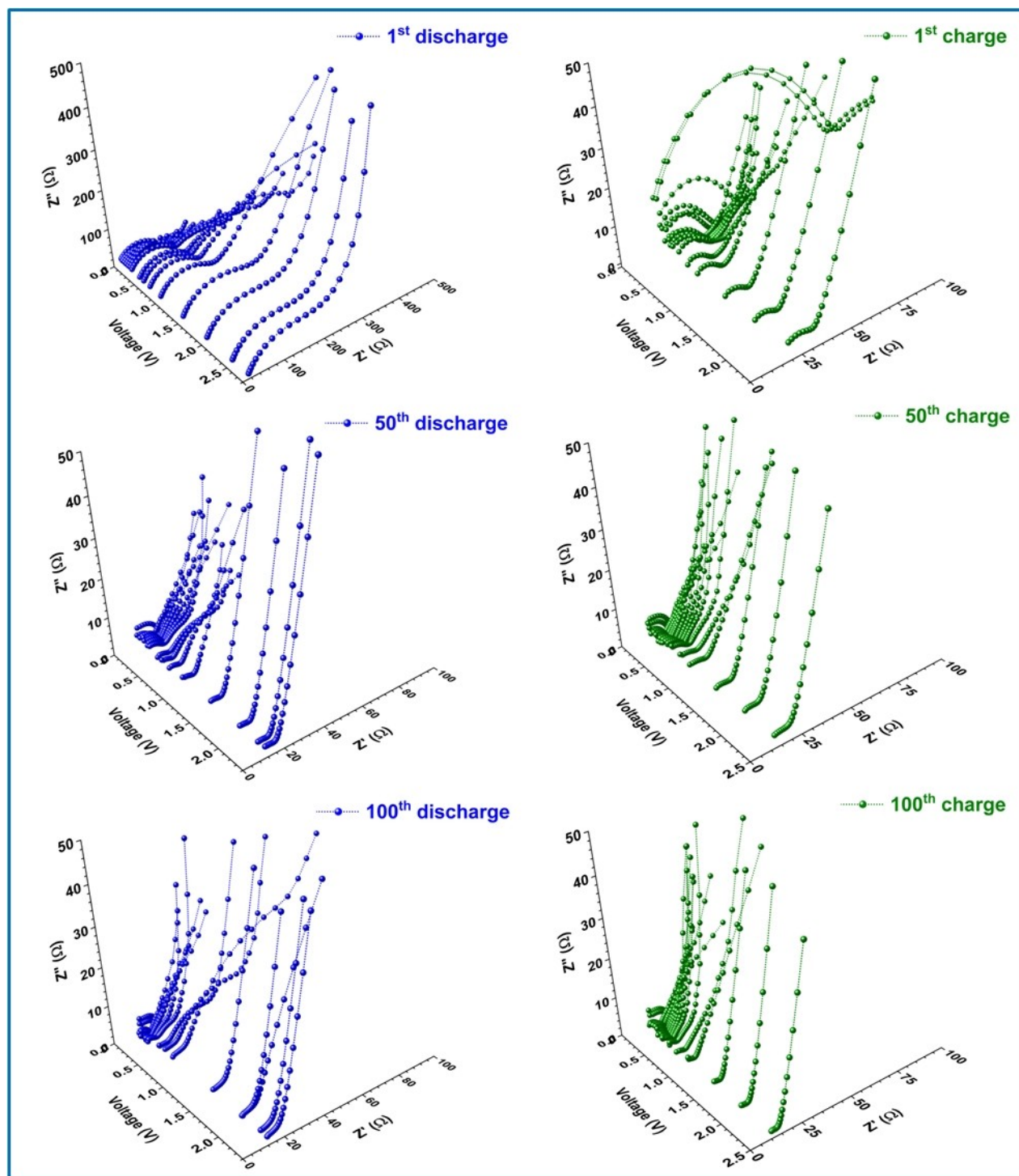


**Figure 5.** In-situ-electrochemical impedance spectroscopy (in-situ-EIS) profile of the Li/RG(75):SiO(25) half-cell. Impedance profile at different potentials of the 1<sup>st</sup>, 50<sup>th</sup>, and 100<sup>th</sup> cycle.

In the full-cell combination with AC, the RG(75): SiO(25) composite displayed superior performance when it comes to energy density, power density, and long-term cyclic stability. The LIC with this particular composite delivered a maximum energy density of 218 Wh kg<sup>-1</sup> and power density of 8.45 kW kg<sup>-1</sup> with long-term cyclic stability for more than 20,000 charge/discharge cycles. The rate performance and long-

term cyclic stability were also tested at different temperature conditions (10, 25, and 40 °C) to analyze its adaptability to various climatic conditions. An excellent performance was observed as the LIC maintained comparable energy and power densities at different temperatures. From this, we observe that the alloying-intercalation synergic effect can bring the best out of the anode materials, and the hybrid capacitors' overall

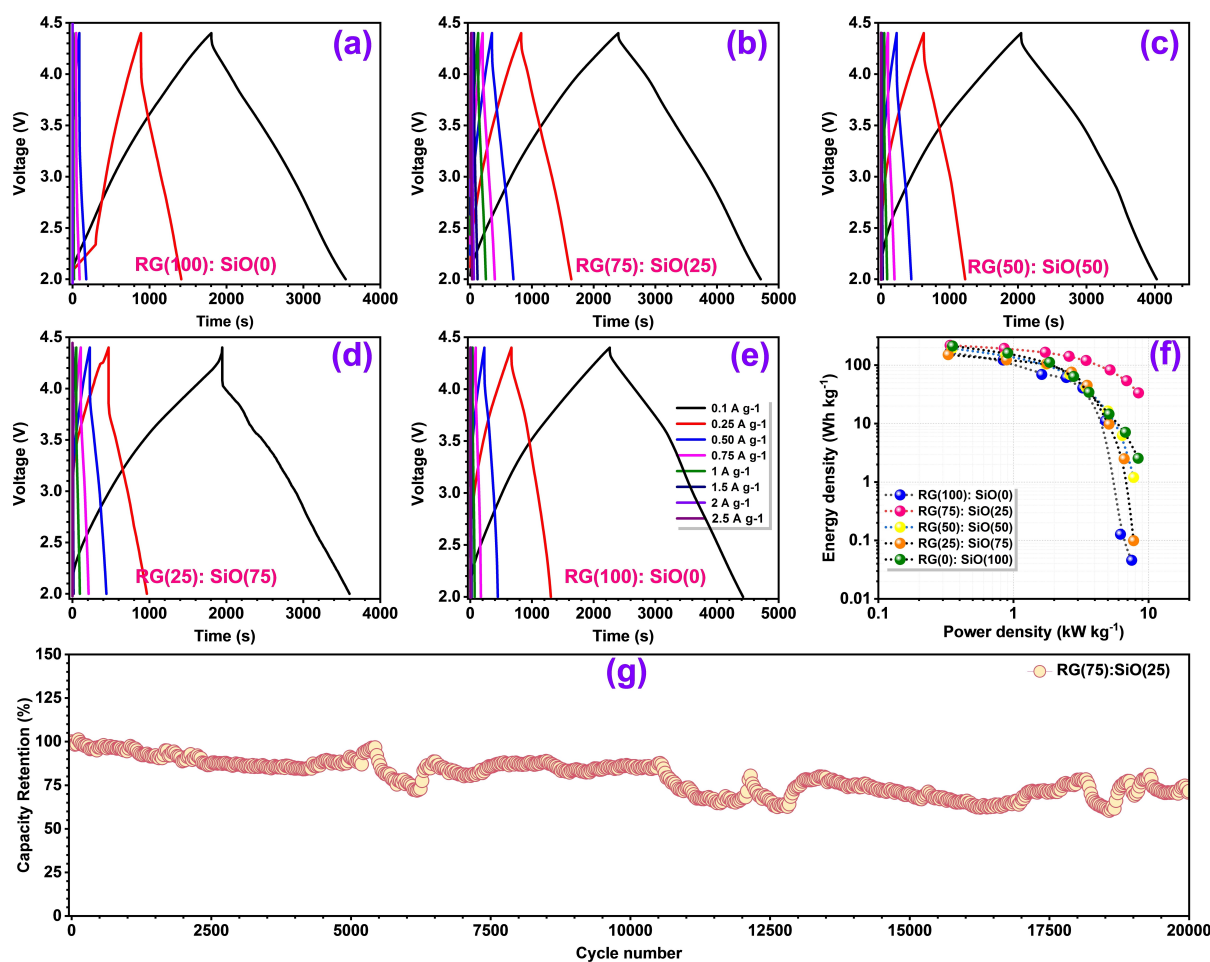


**Figure 6.** Electrochemical performance of the RG:SiO<sub>x</sub> composite LICs: (a–e) Galvanostatic charge-discharge of the different composites at the different current rates, (f) Ragone plot of the different composites, and (g) long-term cycling performance of RG(75):SiO(25) LIC at room temperature at the current rate of 0.75 A g<sup>−1</sup>.

electrochemical performance can be significantly enhanced. Moreover, recovering valuable materials such as graphite provides a direction to the circular economy.

## Experimental Section

### Preparation of RG:SiO<sub>x</sub> Composite

Easy steps were employed to prepare the RG:SiO<sub>x</sub> composite. The graphite is recovered from the spent LIBs using a simple and environmentally friendly approach discussed in our previous works. The RG and commercially available SiO<sub>x</sub> were well-ball-milled inside the planetary ball miller for 10 min with 1:20 as material: balls ratio. The composite were prepared in five different ratios and are RG(0):SiO(100), RG(25):SiO(75), RG(50):SiO(50), RG(75):SiO(25) and RG(100):SiO(0).

### Materials Characterization

The powder X-ray diffraction analysis for RG was performed from 10 to 80° at a 0.5° min.<sup>−1</sup> scan rate using Rigaku D/teX Ultra 250 diffractometer (40 kV, 200 mA, λ = 1.5406 Å) with Cu Kα radiation. The Raman Spectroscopic analysis for the composite was carried out using Lab Ram HR800 UV Raman microscope (Horiba Jobin-Yvon, France) with a 515 nm Diode laser as an excitation light source. Field-emission scanning electron microscope (FE-SEM Gemini560, Germany) measures the surface morphology of all the composites, and the internal structure analysis was carried out using the High-resolution transmission electron microscope (HR-TEM, TECNAI, Philips, the Netherlands, 200 keV). The surface electronic configuration analysis was performed using X-ray photoelectron spectroscopy (XPS, Multilab 2000, UK; monochromatic Al Kα radiation hν = 1486.6 eV). The elemental composition of the composites was analyzed from the Energy-dispersive X-ray spectroscopy (EDS) studies.



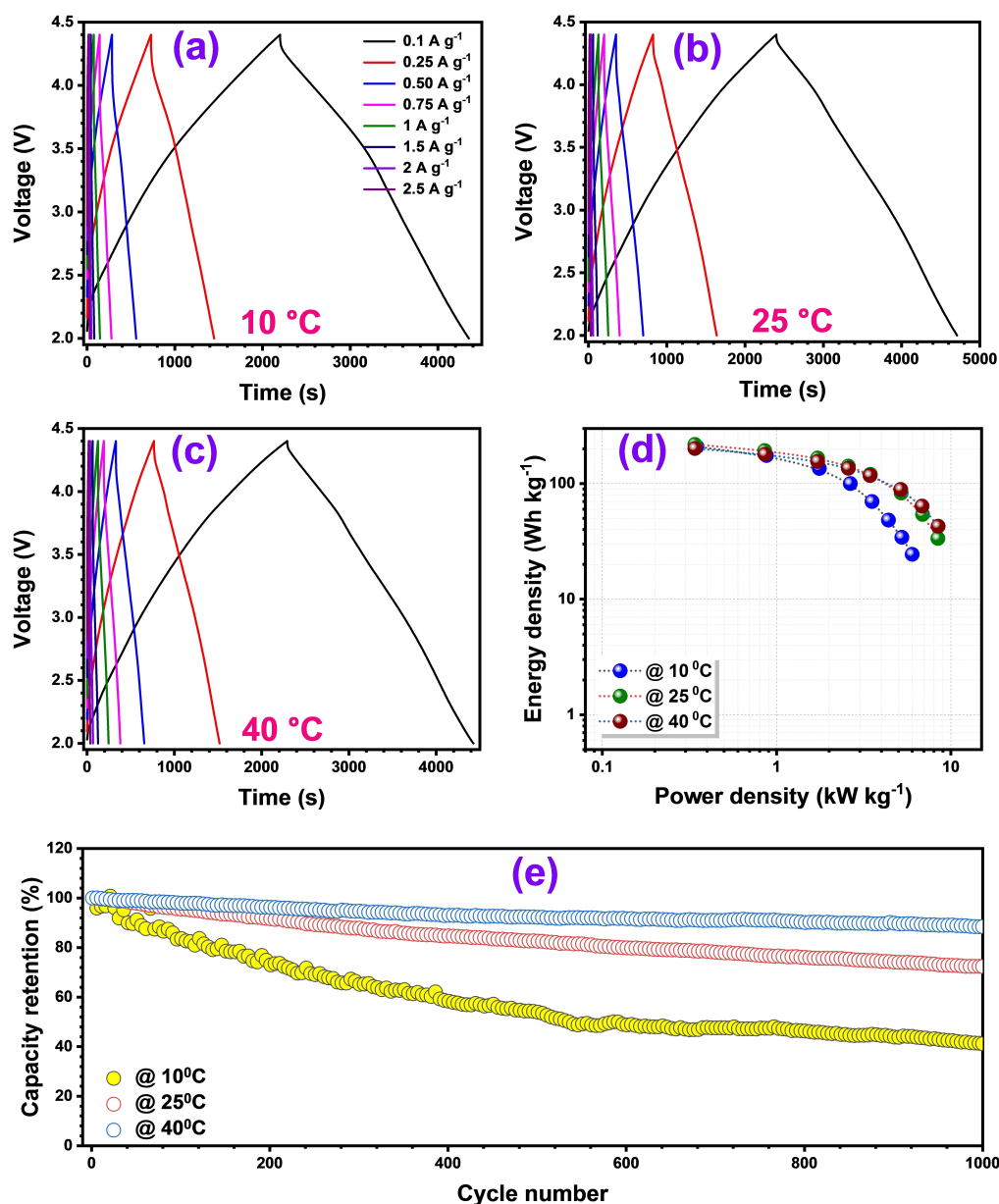


**Figure 7.** Electrochemical performance of RG(75):SiO(25) LIC: (a–c) Galvanostatic charge-discharge at different temperatures (10, 25 & 40 °C) with different current rates, (d) Ragone plot at three different temperatures, and (e) long-term cycling performance at the different temperature at a current density of 1 A g<sup>-1</sup>.

## Electrochemical Studies

The electrodes of all five composites were fabricated using the conventional slurry coating method. The slurry for the composites was prepared by mixing the 80% active material (different composites), 10% conductive carbon (acetylene black), and 10% binder (Carboxymethyl cellulose, CMC) in water solvent for more than 8 h by continuously stirring. Thus, the homogenous slurry is coated on a 15 μm thick copper foil using the doctor blade apparatus (MSK-AFA-III Automatic Thick Film Coater (MTI Corporation)). It is then dried in a hot air oven at 65 °C for 4 h. The uniformly coated dried active material is then rolled on a roll press (Tester Sangyo, Japan). The electrodes of 12 mm

diameter are punched out from it using the photographic electrode cutter. On the other hand, the activated carbon (AC, Kuraray, Japan) electrodes are prepared by a simple hand-made method. Here, 8 mg of AC is mixed with 1 mg of acetylene black and 1 mg of teflonized acetylene black (TAB-2) binder with ethanol solvent in a mortar pestle to form a free-standing film. The film is then pressed on a 14 mm stainless steel current collector (Goodfellow, UK). The composite and AC electrodes are dried in a vacuum oven at 75 °C for over 4 h.

All the cells (both half cells and full cells are fabricated inside the Argon-filled glove box (MBraun, Germany) where the O<sub>2</sub> level < 0.1 ppm and H<sub>2</sub>O level < 0.1 ppm by using CR2016 type coin cells. 1 M LiPF<sub>6</sub> in FEC was the electrolyte used; the

anode and cathode were separated from contact using the Whatman paper (1825-047, GF/F) separator. Lithium metal was the counter/reference electrode for both the composite and AC half cells. The Li/RG:SiO<sub>x</sub> half cells are pre-lithiated prior to the fabrication of AC/RG:SiO<sub>x</sub> full cells. The half-cells are subjected to 3 cycles and dismantled inside the glove box at the discharged state (LiC<sub>6</sub> + Li<sub>3.75</sub>Si + Li<sub>2</sub>O). It is then paired with the mass-balanced AC cathode to get the AC/RG:SiO<sub>x</sub> hybrid capacitor. The AC/RG:SiO<sub>x</sub> full cell is fabricated only after balancing the mass between the two electrodes. A simple equation performs the mass balancing:

$$M_1C_1 = M_2C_2$$

M<sub>1</sub> & M<sub>2</sub> are masses, and C<sub>1</sub> & C<sub>2</sub> are specific capacities of RG:SiO<sub>x</sub> composites and AC, respectively. The electrochemical studies, such as the galvanostatic charge-discharge (GCD) and Electrochemical impedance spectroscopy (EIS), were performed using the Biologic BCS 805 (France) battery tester and the Cyclic voltammetry (CV) analysis by using an electrochemical workstation (Solartron, UK).

## Acknowledgments

YSL acknowledges the financial support from the National Research Foundation of Korea (NRF) grant funded by the Korean government (Ministry of Science, ICT & Future Planning) (No. RS-2023-00208361). VA acknowledges financial support from the Anusandhan National Research Foundation (ANRF), Govt. of India, through Swarnajayanti Fellowship (SB/SJF/2020-21/12).

## Conflict of Interests

The authors declare no conflict of interest.

## Data Availability Statement

The data that support the findings of this study are available from the corresponding author upon reasonable request.

**Keywords:** Li-ion capacitors · Alloy anode · Insertion process · Recycling LIBs · Pre-lithiation

- [1] N. Nitta, F. Wu, J. T. Lee, G. Yushin, *Mater. Today* **2015**, *18*(5), 252–264, <https://doi.org/10.1016/j.mattod.2014.10.040>.
- [2] M. Li, J. Lu, Z. Chen, K. Amine, *Adv. Mater.* **2018**, *30*(33), 1800561, <https://doi.org/10.1002/adma.201800561>.
- [3] J. Xie, Y.-C. Lu, *Nat. Commun.* **2020**, *11*(1), 2499, <https://doi.org/10.1038/s41467-020-16259-9>.

- [4] Muzaffar, A.; Ahamed, M. B.; Deshmukh, K.; Thirumalai, J., *Renew. Sustain. Energy Rev.* **2019**, *101* (July 2018), 123–145, <https://doi.org/10.1016/j.rser.2018.10.026>.
- [5] M. Soltani, S. H. Beheshti, *J. Energy Storage* **2021**, *34*, 102019, <https://doi.org/10.1016/j.est.2020.102019>.
- [6] N. Omar, J. Ronsmans, Y. Firozu, M. A. Monem, A. Samba, H. Gualous, O. Hegazy, J. Smekens, T. Coosemans, P. Van Den Bossche, J. Van Mierlo, *2013 World Electr. Veh. Symp. Exhib. EVS 2014* **2014**, 1–11, <https://doi.org/10.1109/EVS.2013.6914718>.
- [7] D. P. Dubal, O. Ayyad, V. Ruiz, P. Gómez-Romero, *Chem. Soc. Rev.* **2015**, *44*(7), 1777–1790, <https://doi.org/10.1039/c4cs00266k>.
- [8] V. Aravindan, Y.-S. Lee, *J. Phys. Chem. Lett.* **2018**, *9*(14), 3946–3958, <https://doi.org/10.1021/acs.jpclett.8b01386>.
- [9] M. Akshay, S. Jayaraman, M. Ulaganathan, Y.-S. Lee, V. Aravindan, *J. Colloid Interface Sci.* **2023**, *646*, 703–710, <https://doi.org/10.1016/j.jcis.2023.05.091>.
- [10] M. Akshay, S. Praneetha, Y.-S. Lee, V. Aravindan, *Electrochim. Acta* **2023**, *439*, 141599, <https://doi.org/10.1016/j.electacta.2022.141599>.
- [11] W.-J. Zhang, *J. Power Sources* **2011**, *196*(1), 13–24, <https://doi.org/10.1016/j.jpowsour.2010.07.020>.
- [12] G. G. Eshetu, H. Zhang, X. Judez, H. Adenusi, M. Armand, S. Passerini, E. Figgemeier, *Nat. Commun.* **2021**, *12*(1), 1–14, <https://doi.org/10.1038/s41467-021-25334-8>.
- [13] X. Xia, X. Qian, C. Chen, W. Li, D. He, G. He, H. Chen, *J. Energy Storage* **2023**, *72*, 108715, <https://doi.org/10.1016/j.est.2023.108715>.
- [14] C. Zhang, F. Wang, J. Han, S. Bai, J. Tan, J. Liu, F. Li, *Small Struct.* **2021**, *2*(6), 2100009, <https://doi.org/10.1002/ssstr.202100009>.
- [15] D. Ma, Z. Cao, A. Hu, *Nano-Micro Lett.* **2014**, *6*(4), 347–358, <https://doi.org/10.1007/s40820-014-0008-2>.
- [16] M. Akshay, R. Belgamwar, S. Praneetha, V. Polshettiwar, V. Aravindan, *ACS Mater. Lett.* **2023**, *5*(3), 715–721, <https://doi.org/10.1021/acsmaterialslett.2c01224>.
- [17] S. Natarajan, D. Shanthana Lakshmi, H. C. Bajaj, D. N. Srivastava, *J. Environ. Chem. Eng.* **2015**, *3*(4, Part A), 2538–2545, <https://doi.org/10.1016/j.jece.2015.09.011>.
- [18] G. Park, Y. Choi, S. Shin, Y. Lee, S. Hong, *ACS Appl. Mater. Interfaces* **2022**, *14*(27), 30639–30648, <https://doi.org/10.1021/acsami.2c01460>.
- [19] Z. L. Wu, S. B. Ji, L. K. Liu, T. Xie, L. Tan, H. Tang, R. G. Sun, *Rare Met.* **2021**, *40*(5), 1110–1117, <https://doi.org/10.1007/s12598-020-01445-x>.
- [20] X. Feng, J. Yang, Q. Lu, J. Wang, Y. Nuli, *Phys. Chem. Chem. Phys.* **2013**, *15*(34), 14420–14426, <https://doi.org/10.1039/c3cp51799c>.
- [21] L. Hu, W. Xia, R. Tang, R. Hu, L. Ouyang, T. Sun, H. Wang, *Front. Chem.* **2020**, *8*(May), 1–8, <https://doi.org/10.3389/fchem.2020.00388>.
- [22] M. S. Al Ja'farawy, D. N. Hikmah, U. Riyadi, A. Purwanto, H. Widiyandari, *J. Electron. Mater.* **2021**, *6667*–6687, <https://doi.org/10.1007/s11664-021-09187-x>.
- [23] Y.-F. Meng, H.-J. Liang, C.-D. Zhao, W.-H. Li, Z.-Y. Gu, M.-X. Yu, B. Zhao, X.-K. Hou, X.-L. Wu, *J. Energy Chem.* **2022**, *64*, 166–171, <https://doi.org/10.1016/j.jechem.2021.04.047>.
- [24] S.-H. Zheng, X.-T. Wang, Z.-Y. Gu, H.-Y. Lü, X.-Y. Zhang, J.-M. Cao, J.-Z. Guo, X.-T. Deng, Z.-T. Wu, R.-H. Zeng, X.-L. Wu, *J. Power Sources* **2023**, *587*, 233697, <https://doi.org/10.1016/j.jpowsour.2023.233697>.
- [25] M. Du, K.-D. Du, J.-Z. Guo, Y. Liu, V. Aravindan, J.-L. Yang, K.-Y. Zhang, Z.-Y. Gu, X.-T. Wang, X.-L. Wu, *Rare Met.* **2023**, *42*(5), 1603–1613, <https://doi.org/10.1007/s12598-022-02230-8>.
- [26] M. L. Divya, S. Natarajan, Y.-S. Lee, V. Aravindan, *J. Mater. Chem. A* **2020**, *8*(9), 4950–4959, <https://doi.org/10.1039/C9TA13913C>.
- [27] M. L. Divya, S. Natarajan, Y.-S. Lee, V. Aravindan, *ChemSusChem* **2020**, *13*(21), 5654–5663, <https://doi.org/10.1002/cssc.202001355>.
- [28] J. Asenbauer, T. Eisenmann, M. Kuenzel, A. Kazzazi, Z. Chen, D. Bresser, *Energy Fuels* **2020**, *4*(11), 5387–5416, <https://doi.org/10.1039/D0SE00175A>.

Manuscript received: April 16, 2024  
Revised manuscript received: October 19, 2024  
Accepted manuscript online: December 8, 2024  
Version of record online: December 19, 2024